applied sciences

MDPI

Article

Analysis and Application of Dual-Control Single-Exponential Water Inrush Prediction Mechanism for Excavation Roadways Based on Peridynamics

Xiaoning Liu [1,2], Xinqiu Fang [1,*], Minfu Liang [1], Gang Wu [1,*], Ningning Chen [1] and Yang Song [1]

[1] School of Mining Engineering, China University of Mining and Technology, Xuzhou 221116, China; cumtlxn@foxmail.com (X.L.); liangmf2014@cumt.edu.cn (M.L.); ningningchen@cumt.edu.cn (N.C.)
[2] Safety Training Center of Shanxi Bureau, National Mine Safety Administration, Taiyuan 030012, China
* Correspondence: xinqiufang@cumt.edu.cn (X.F.); wu007gang007@cumt.edu.cn (G.W.)

Featured Application

The proposed prediction model provides a practical tool for assessing water inrush risk in coal mine roadways during excavation. It aids in implementing targeted water hazard prevention strategies, ultimately contributing to reducing water-related accidents in underground coal mines.

Abstract

Roof water inrush accidents in coal mine driving roadways occur frequently in China, accounting for a high proportion of major coal mine water hazard accidents and causing serious losses. Aiming at the lack of research on the mechanism of roof water inrush in driving roadways and the difficulty of predicting water inrush accidents, this paper constructs a local damage criterion for coal–rock mass and a seepage–fracture coupling model based on peridynamics (PD) bond theory. It identifies three zones of water-conducting channels in roadway surrounding rock, the water fracture zone, the driving fracture zone, and the water-resisting zone, revealing that the damage degree of the water-resisting zone dominates the transformation mechanism between delayed and instantaneous water inrush. A discriminant function for the effectiveness of water-conducting channels is established, and a single-index prediction and evaluation system based on damage critical values is proposed. A "geometry damage" dual-control water inrush prediction model within the PD framework is constructed, along with a non-local action mechanism model and quantitative prediction method for water inrush. Case studies verify the threshold for delayed water inrush and criteria for instantaneous water inrush. The research results provide theoretical tools for roadway water exploration design and water hazard prevention and control.

Keywords: local damage criterion for coal–rock mass; critical damage threshold of water-resisting zone; dual-control water inrush prediction model; single-exponential water inrush prediction method

check for updates

Academic Editor: Tiago Filipe da Silva Miranda

Received: 12 June 2025
Revised: 2 July 2025
Accepted: 4 July 2025
Published: 7 July 2025

Citation: Liu, X.; Fang, X.; Liang, M.; Wu, G.; Chen, N.; Song, Y. Analysis and Application of Dual-Control Single-Exponential Water Inrush Prediction Mechanism for Excavation Roadways Based on Peridynamics. *Appl. Sci.* **2025**, *15*, 7621. https://doi.org/10.3390/app15137621

Copyright: © 2025 by the authors. Licensee MDPI, Basel, Switzerland. This article is an open access article distributed under the terms and conditions of the Creative Commons Attribution (CC BY) license (https://creativecommons.org/licenses/by/4.0/).

1. Introduction

In major coal mine water hazard accidents of China, roof water inrush from driving roadways accounts for a significant proportion and causes severe losses [1–4]. Based on the author's investigation, statistics, and analysis of major and above-level water inrush accidents in Chinese coal mines from 1977 to 2024, specifically focusing on roof water inrush incidents in development headings, it was found that 84 major and above-level water

inrush accidents occurred nationwide during this period, resulting in 1810 fatalities and missing persons; notably, 38 such accidents were attributed to roof water inrush in development headings, causing 856 fatalities and missing persons, accounting for 45.24% of the total major water inrush accidents and 47.29% of the associated casualties, respectively. The average fatality rate per roof water inrush accident was 22.53, slightly exceeding the overall major water inrush average of 21.55 fatalities per accident. Analysis of these 38 roof water inrush accidents revealed that, with respect to geological controls, 33 accidents (86.84%) were non-structurally controlled, while only 5 (13.16%) were structurally controlled; regarding temporal patterns, instantaneous-type inrushes predominated (29 accidents, 76.32%), followed by delayed-type (8 accidents, 21.05%), with intermittent-type being minimal (1 accident, 2.63%). Consequently, roof water inrush accidents in development headings constitute a significant proportion of major water inrush disasters in Chinese coal mines, exhibiting well-defined characteristics concerning both their likelihood of occurrence and the severity of consequences. Affected by structural planes such as joints and fractures, the mechanical structure of the surrounding rock in driving roadways exhibits obvious discontinuous phenomena from macro- to micro-scales, and traditional continuous medium mechanics theories can no longer fully explain the mechanism of fracture evolution. Current methodologies for predicting and evaluating mine water inrush disasters [5–7], such as vulnerability index approaches based on hydrogeological parameters and empirical water inrush coefficient models, primarily depend on static geological exploration data and experiential formulas for risk zoning and threshold determination. These approaches exhibit pronounced limitations in assessing excavation roadway water inrush risks due to their inability to (i) accurately quantify activation risks of concealed water-bearing structures or critical conditions for water-conducting channel formation under dynamic excavation-induced disturbances, leading to inadequate precision for localized high-risk zones; (ii) dynamically integrate real-time excavation data to update aquiclude evaluations, resulting in prediction outcomes that lag behind advancing workfaces; (iii) achieve sufficient spatial resolution for short-range, high-risk target identification ahead of excavation roadways, given their regional-scale evaluation framework; and (iv) ensure model generalizability, as empirical thresholds derived from specific mining districts frequently cause misjudgments or missed alerts when extrapolated to new contexts. Consequently, prevailing methods demonstrate fundamental bottlenecks in addressing the complex, dynamic, and spatially localized nature of water inrush hazards during roadway excavation. While peridynamics demonstrates unique advantages in predicting discontinuous failure of rock masses [8–10], its application to the evolution of water inrush channels remains unresolved. The objective of this study is to develop and validate a dual-control (geometry damage) water inrush prediction model based on peridynamics theory, aimed at improving the accuracy of water hazard prediction and prevention in coal mine roadway.

2. Methodology

2.1. Peridynamics Damage Criterion of Coal–Rock Mass

Peridynamics (PD), an emerging non-local mechanics theory proposed by Professor Silling in 2000 that is continuously developing, can describe a series of mechanical behaviors of coal and rock masses from continuous to discontinuous and from micro- to macro-scales through the non-local theory [8–10]. This avoids the complexity of traditional discontinuous multi-scale models.

In PD theory, the interaction force (also known as bond force) between material points x and x′ within neighborhood radius δ (horizon) is expressed in an integral form. The dynamic equation of the material point x can be written as

$$\rho(x)\ddot{u}(x,t) = \int_{H_x} f(x',x,t)dV_{x'} + b(x,t) \tag{1}$$

In the formula, ρ represents the mass density of the material;

u represents the displacement of the material point;

$\ddot{u}(x,t) = \frac{\partial^2 u(x,t)}{\partial t^2}$ represents the acceleration of the material point;

b (x, t) represents the body force density of external loads;

$H_x = H(x,\delta) = \{|x' - x| \le \delta | x' \in \Omega\}$ denotes the set of material points in the spatial domain Ω centered at the material point x (i.e., the near-field domain of the material point x), where δ is the neighborhood radius;

$f(x',x,t)$ represents the interaction between the material points x and x′, with the dimension of force density. The expression of $f(x',x,t)$ is given by the following formula:

$$f(x',x,t) = t(x',x,t) - t(x,x',t) \tag{2}$$

$$t(x',x,t) = \underline{T}[x,t]\langle x' - x\rangle \tag{3}$$

$$t(x,x',t) = \underline{T}[x',t]\langle x - x'\rangle \tag{4}$$

In the formula, $\underline{T}$ represents the vector force state, the quantities affecting this state are indicated within, and the mapping or action object of this state is shown within < >.

The force state acts on the relative position x′ − x between a point and any other point within its vicinity, resulting in a force density vector t. This form ensures the conservation of momentum for the entire system. Thus, dynamic Equation (1) for material point x can be expressed as

$$\begin{aligned} \rho(x)\ddot{u}(x,t) = \quad & \int_{H_x} \{\underline{T}[x,t]\langle x' - x\rangle - \underline{T}[x',t]\langle x - x'\rangle\} dV_{x'} \\ & + b(x,t) \end{aligned} \tag{5}$$

Key-type PD theory can be regarded as a special case of state-type PD theory:

$$t(x',x,t) = -t(x,x',t) = \frac{1}{2} f(x',x,t) = -\frac{1}{2} f(x',x,t) \tag{6}$$

Therefore, on the basis of Equation (5), the force vector state of the material point can be uniformly expressed as follows:

$$\underline{T}[x,t]\langle x' - x\rangle = \underline{t}\langle\xi\rangle \underline{M}(\underline{Y})\, \underline{M} = \frac{\underline{Y}}{|\underline{Y}|} \tag{7}$$

$$\xi = x' - x \quad \eta = u' - u \tag{8}$$

In the formula, $\underline{t}$ represents the magnitude of the force density; $\underline{M}$ represents the direction of the force density; $\underline{Y}$ represents the deformation; and ξ and η, respectively, represent the initial position vector (the initial length of the bond) and the relative displacement vector of the material point.

In the key-type PD theory, the force density between material points is equal in magnitude and opposite in direction, so the force density can be expressed as

$$\underline{t}\langle\xi\rangle = \begin{cases} ce & (\text{when } |x' - x| \le \delta) \\ 0 & (\text{otherwise}) \end{cases} \tag{9}$$

In the formula, c represents the microscopic elastic parameter of the substance, called the micromodulus, and e represents the elongation of the bond.

Based on the principle of strain energy density equivalence, an expression for PD bond-type micromodulus c is established through traditional continuum mechanics:

$$c = \begin{cases} \frac{3E}{h\delta^3} & (\text{one dimension}) \\ \frac{8E}{\pi h\delta^4(1-\nu)} & (\text{plane stress}) \\ \frac{8E}{\pi h\delta^4(1-\nu-2\nu^2)} & (\text{plane strain}) \\ \frac{15E}{2\pi h\delta^5(1-2\nu)} & (\text{three dimensions}) \end{cases} \tag{10}$$

In the formula, E is the elastic modulus of coal–rock mass, ν is the Poisson ratio, h is the continuous thickness at the particle point, and δ is the neighborhood radius.

The criterion for the destruction of the key is an important theoretical basis for analyzing the generation and expansion of damage fractures in coal–rock mass through PD key-type analysis. It can be assumed that when the elongation rate $|s|$ of the key reaches the critical elongation rate s0, the key will break irreversibly. That is,

$$|s| \geq s_0 \tag{11}$$

The elongation of the key is $|s|$:

$$|s| = \frac{e}{|\xi|} = \frac{|\xi + \eta| - |\xi|}{|\xi|} \tag{12}$$

The critical elongation s_0 can be obtained according to the critical energy release rate G_0 of coal–rock mass:

$$s_0 = \frac{6G_0}{\pi\delta^3\xi|\underline{t}\langle\xi\rangle - \underline{t}\langle-\xi\rangle|} \tag{13}$$

At the same time, in order to describe and characterize the damage of coal–rock mass from microcracking (microscopic initiation) and fissure (microscopic expansion) to macrofracturing (macroscopic damage), a local damage concept of PD bond-type material point is established, that is, the ratio of the number of broken bonds to the total number of bonds within the near field.

$$\mathrm{D}(\mathrm{x},t) = \frac{\int_{\mathrm{H_x}} (1 - \varphi(\mathrm{x}',\mathrm{x},t))dV_{\mathrm{x}'}}{\int_{\mathrm{H_x}} dV_{\mathrm{x}'}} \tag{14}$$

In the formula,

$$\varphi(\mathrm{x}',\mathrm{x},t) = \begin{cases} 1 & (|s| < s_0) \\ 0 & (|s| \geq s_0) \end{cases} \tag{15}$$

Equation (15) indicates that in the PD bond type, there are only two states of bond destruction and non-destruction for the same material point in the near field, and there is no intermediate state.

Due to the extensive presence of discontinuous structures such as pores, joints, and fractures within coal rock bodies, the seepage flow exhibits non-uniformity and anisotropy [11–13]. The seepage flow foundation model primarily comprises an equivalent continuous medium based on representative units, a discrete fracture network based on fracture seepage, and a dual medium based on pore–fracture seepage.

2.2. Equivalent Continuous Porous Medium Model

Using the fundamental principles of near-field dynamics in simulating medium transmission, a near-field dynamics model for equivalent continuous medium seepage problems

is established. In this model, a material point x interacts with all other material points x within its neighborhood through bonds. By treating some material points as water storage points and their neighboring bonds as water conduits, the seepage process of groundwater in porous media can be simulated. The hydraulic potential energy difference between the water storage points at both ends of the bond represents the driving force for water flow. The volumetric flow rate of water transferred between two water storage points via the bond can be calculated using Darcy's law:

$$u_{\mathrm{b}}\left[\mathrm{x_i}, \mathrm{x_j}\right] = -\frac{k_{\mathrm{b}}\left[\mathrm{x_i}, \mathrm{x_j}\right]}{\mu}\left(\frac{\Phi\left[\mathrm{x_j}\right] - \Phi\left[\mathrm{x_i}\right]}{\left\|\xi_{\mathrm{x_i x_j}}\right\|}\right)\mathrm{e}\left[\mathrm{x_i}, \mathrm{x_j}\right] \tag{16}$$

In the formula, Φ represents the hydraulic potential energy of any water storage point in the coal mass, μ represents the fluid viscosity, k_{b} represents the permeability of the key (the value depends on the macroscopic permeability of the coal mass), and $e\left[\mathrm{x_i}, \mathrm{x_j}\right] = \xi_{\mathrm{x_i x_j}} / \left|\left|\xi_{\mathrm{x_i x_j}}\right|\right|$ represents the unit length along the direction of the key.

The mass flow rate of the bond can be obtained by multiplying the volume flow rate by fluid density ρ:

$$q_{\mathrm{b}}\left[\mathrm{x_i}, \mathrm{x_j}\right] = -\rho\left[\mathrm{x_i}, \mathrm{x_j}\right]\frac{k_{\mathrm{b}}\left[\mathrm{x_i}, \mathrm{x_j}\right]}{\mu}\left(\frac{\Phi\left[\mathrm{x_j}\right] - \Phi\left[\mathrm{x_i}\right]}{\left\|\xi_{\mathrm{x_i x_j}}\right\|}\right)\mathrm{e}\left[\mathrm{x_i}, \mathrm{x_j}\right] \tag{17}$$

The amount of water transmitted by the storage point should also satisfy the law of conservation of matter, that is,

$$\frac{\partial}{\partial \mathrm{t}}\left(\rho\left[\mathrm{x_i}, \mathrm{x_j}\right]\varphi_{\mathrm{b}}\left[\mathrm{x_i}, \mathrm{x_j}\right]\right) = \frac{q_{\mathrm{b}}\left[\mathrm{x_i}, \mathrm{x_j}\right] \cdot \left(-A_{\mathrm{b}}\mathrm{e}\left[\mathrm{x_i}, \mathrm{x_j}\right]\right)}{A_{\mathrm{b}}\left\|\xi_{\mathrm{x_i x_j}}\right\|} + R_{\mathrm{b}}\left[\mathrm{x_i}, \mathrm{x_j}\right] \tag{18}$$

In the formula, φ_{b} [$\mathrm{x_i}$, $\mathrm{x_j}$] represents the porosity of the key, A_{b} represents the cross-section of the key, and R_{b} [$\mathrm{x_i}$, $\mathrm{x_j}$] represents the source sink term.

Integrate over the domain of water storage point x_{i}. Assuming the volumetric flow density of water storage point x_{i} is the average of the volumetric flow densities of all connected keys within its neighborhood, and the source–sink term of water storage point xi is the average of all connected keys within its neighborhood, the total fluid flow of all related keys at x_{i} can be derived. Thus, the mass conservation equation for water storage point x_{i} is

$$\frac{\partial}{\partial \mathrm{t}}\left(\rho\left[\mathrm{x_i}\right]\varphi\left[\mathrm{x_i}\right]\right) = \int_{\mathrm{H_x}} k\left[\mathrm{x_i}, \mathrm{x_j}\right]\frac{\rho\left[\mathrm{x_i}, \mathrm{x_j}\right]}{\mu}\frac{\Phi\left[\mathrm{x_j}\right] - \Phi\left[\mathrm{x_i}\right]}{\left\|\xi_{\mathrm{x_i x_j}}\right\|^2}dV_{\mathrm{x_j}} + R\left[\mathrm{x_i}\right] \tag{19}$$

In the formula,

k [$\mathrm{x_i}$, $\mathrm{x_j}$] = k_{b} [$\mathrm{x_i}$, $\mathrm{x_j}$]/$V_{\mathrm{x_i}}$. The microscopic permeability function of the key related to the macroscopic permeability of coal-bearing rocks is shown.

In the case of steady-state seepage, the relationship between the near-field dynamic micropermeability and macroscopic permeability of coal–rock mass under different influence functions is derived:

$$k_b\left[\mathrm{x_i}, \mathrm{x_j}\right] = \begin{cases} \frac{4k}{\pi\delta^2} & (\omega = 1) \\ \frac{12k}{\pi\delta^2}\left(1 - \frac{\left\|\xi_{\mathrm{x_i x_j}}\right\|}{\delta}\right) & \left(\omega = 1 - \frac{\left\|\xi_{\mathrm{x_i x_j}}\right\|}{\delta}\right) \\ \frac{2k}{\pi\delta}\frac{1}{\left\|\xi_{\mathrm{x_i x_j}}\right\|} & \left(\omega = \frac{1}{\left\|\xi_{\mathrm{x_i x_j}}\right\|}\right) \end{cases} \tag{20}$$

On the basis of the above analysis, the basic near-field dynamic equations of the unidirectional flow process in isotropic porous uniform medium can be obtained:

(1) Uniform type ($\omega = 1$)

$$\frac{\partial}{\partial t}(\rho[x_i]\varphi[x_i]) = \int_{H_x} \frac{\rho[x_i, x_j]}{\mu} \frac{4k}{\pi\delta^2} \frac{\Phi[x_j] - \Phi[x_i]}{\left\|\xi_{x_i x_j}\right\|^2} dA_{x_j} + R[x_i] \tag{21}$$

(2) Linear model ($\omega = 1 - \left\|\xi_{x_i x_j}\right\|/\delta$)

$$\frac{\partial}{\partial t}(\rho[x_i]\varphi[x_i]) = \int_{H_x} \frac{\rho[x_i, x_j]}{\mu} \frac{12k}{\pi\delta^2} (1 - \frac{\left\|\xi_{x_i x_j}\right\|}{\delta}) \frac{\Phi[x_j] - \Phi[x_i]}{\left\|\xi_{x_i x_j}\right\|^2} dA_{x_j} + R[x_i] \tag{22}$$

(3) Countdown type ($\omega = 1/\left\|\xi_{x_i x_j}\right\|$)

$$\frac{\partial}{\partial t}(\rho[x_i]\varphi[x_i]) = \int_{H_x} \frac{\rho[x_i, x_j]}{\mu} \frac{2k}{\pi\delta} \frac{1}{\left\|\xi_{x_i x_j}\right\|} \frac{\Phi[x_j] - \Phi[x_i]}{\left\|\xi_{x_i x_j}\right\|^2} dA_{x_j} + R[x_i] \tag{23}$$

Through a Matlab program, a uniform isotropic porous homogeneous medium was selected as the object, and a numerical analysis of slow tensile load on microunits containing a single pore was carried out to verify the experimental results.

As shown in Figure 1, a single circular pore micro-element is selected from the microscopic local area of an isotropic homogeneous medium. The origin of the *xOy* coordinate system for this micro-element is the center of the circular pore, with horizontal length *L* and vertical length *W*. The vertical boundary is fixed, while the horizontal boundary is subjected to compression or tension loads, with no other fractures inside. The horizontal length *L* and vertical length *W* of the micro-element are both 50 mm, and the pore diameter *D* is 10 mm. Based on the properties of common coal seam surrounding rocks, the elastic modulus is 30 GPa, Poisson's ratio is 0.33, and the density is 2400 kg/m^3. For the boundary conditions, the vertical boundary is fixed, and a tensile load of 200 MPa is applied to the horizontal boundary. In terms of near-field dynamic discrete parameters, there are 100 material points in the *x* direction, 106 material points in the y direction (with 3 fixed material points at the top and bottom of the vertical boundary), and 1 material point in the z direction. The spacing Δ between material points is 5×10^{-4} m, the volume ΔV of a single material point is 1.25×10^{-10} m^3, and the virtual boundary layer volume $\Delta V\delta$, which is the volume of the upper and lower fixed boundaries, is 3.75×10^{-8} m^3. The neighborhood range δ should be greater than 3Δ, and can be set to 3.014Δ. The critical elongation s_0 is 1 when considering no damage to the near-field interaction bonds of the material points, and 0.02 when considering damage, with 0.02 being used in this unit test.

In this numerical simulation, the adaptive dynamic relaxation method was employed. The critical elongation accounted for damage, with a time step Δt of 1 s and a total calculation time t of 800. As shown in Figure 2, damage between material points is allowed, and the development of damage trends can be observed at different time steps. The numerical simulation of the porous micro-element test served as a good validation.

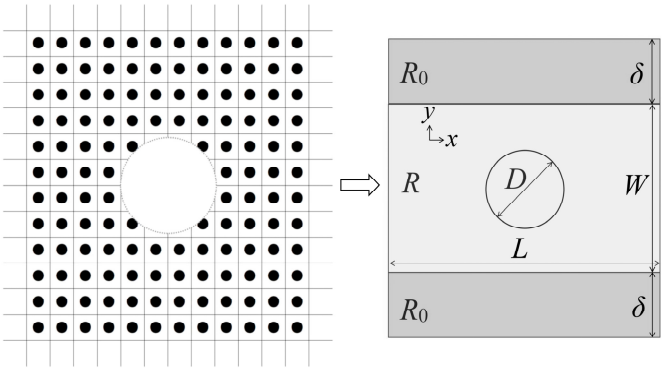


Figure 1. Schematic of calculation model of pore microunit in isotropic homogeneous medium.

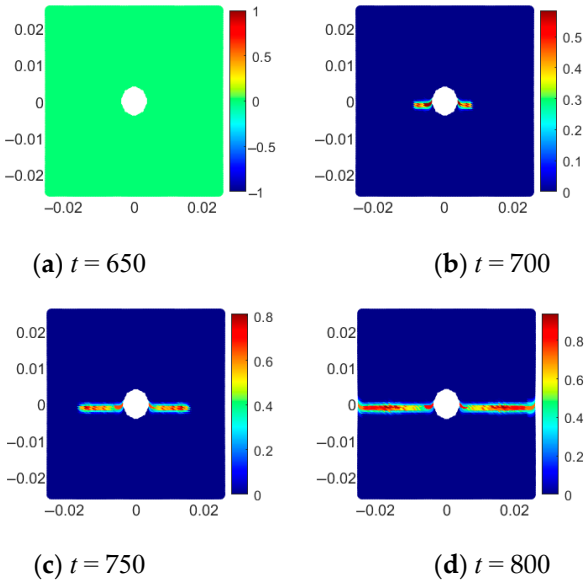


Figure 2. Verification results of numerical simulation of pore microunit deformation at different synchronous displacements.

2.3. Discrete Fracture Network Model

Based on peridynamics, the fracture is abstracted as a discrete network with a certain length, tendency, dip angle, and width, as shown in Figure 3.

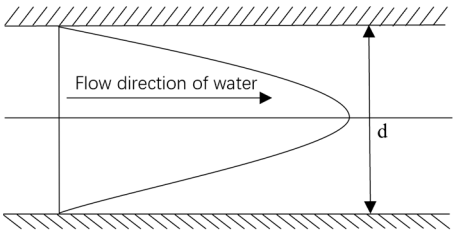


Figure 3. Schematic of plane fissure water flow.

The single micro-fracture of coal–rock mass is simplified into a two-parallel plate structure, and the fluid flow in the fracture follows the Navier—Stokes (N—S) equation [14–16]:

$$\frac{\partial u_i}{\partial t} = F_i - \frac{1}{\rho} P_i + \nu u_{i,j} \tag{24}$$

In the formula, u_{i} represents the component of fluid velocity, F_{i} represents the external force, ρ represents the density of fluid, P_{i} represents the component of fluid pressure, and v represents the kinematic viscosity coefficient of fluid.

When the fluid velocity in the fracture is small, the fluid motion state can be regarded as laminar flow. Since the width of the fracture is constant, the velocity u_x at each point in the x direction is constant. At the same time, the velocity is low, and the velocity head can be ignored. The total head is the sum of the pressure head and the position head, so the above formula is

$$\frac{\mathrm{d}^2 u_x}{\mathrm{d}z^2} = \frac{1}{\rho v}\frac{\mathrm{d}p}{\mathrm{d}x} = \frac{g}{v}\frac{\mathrm{d}p}{\mathrm{d}x} \tag{25}$$

In the water flow of parallel plate fissure, when $z = \pm d/2$ and $u_x = 0$, the velocity distribution can be obtained in the following form:

$$u_x = \frac{g(d^2 - 4z^2)}{8v} J \tag{26}$$

In the formula,

$J = -\frac{\mathrm{d}h}{\mathrm{d}x}$ represents the hydraulic gradient.

The flow through the fracture can be integrated to obtain

$$q = \int_{-\frac{d}{2}}^{\frac{d}{2}} u_x \mathrm{d}z = \frac{g d^3 J}{12v} \tag{27}$$

Rewrite the above equation in the form of Darcy's law:

$$q = k_f \frac{g d J}{v} \tag{28}$$

In the formula,

k_f is the permeability of the fracture, which is proportional to the width of the fracture.

$$k_f = \frac{d^2}{12} \tag{29}$$

Based on the law of conservation of mass, the basic equations of near-field dynamics of seepage in discrete fracture networks can be derived:

(1) Uniform type ($\omega = 1$)

$$\frac{\partial}{\partial \mathrm{t}}(\rho_f[\mathrm{x_i}]\varphi_f[\mathrm{x_i}]) = \int_{\mathrm{H_x}} \frac{\rho_f[\mathrm{x_i}, \mathrm{x_j}]}{\mu_f} \frac{4k_f}{\pi\delta^2} \frac{\Phi_f[\mathrm{x_j}] - \Phi_f[\mathrm{x_i}]}{\left\|\xi_{\mathrm{x_i x_j}}\right\|^2} dA_{\mathrm{x_j}} + R_f[\mathrm{x_i}] \tag{30}$$

(2) Linear model ($\omega = 1 - \left\|\xi_{\mathrm{x_i x_j}}\right\|/\delta$)

$$\frac{\partial}{\partial \mathrm{t}}(\rho_f[\mathrm{x_i}]\varphi_f[\mathrm{x_i}]) = \int_{\mathrm{H_x}} \frac{\rho_f[\mathrm{x_i}, \mathrm{x_j}]}{\mu_f} \frac{12k_f}{\pi\delta^2} \left(1 - \frac{\left\|\xi_{\mathrm{x_i x_j}}\right\|}{\delta}\right) \frac{\Phi_f[\mathrm{x_j}] - \Phi_f[\mathrm{x_i}]}{\left\|\xi_{\mathrm{x_i x_j}}\right\|^2} dA_{\mathrm{x_j}} + R_f[\mathrm{x_i}] \tag{31}$$

(3) Countdown type ($\omega = 1/\left\|\xi_{\mathrm{x_i x_j}}\right\|$)

$$\frac{\partial}{\partial t}(\rho_f[x_i]\varphi_f[x_i]) = \int_{H_x} \frac{\rho_f[x_i, x_j]}{\mu_f} \frac{2k_f}{\pi\delta} \frac{1}{\left\|\xi_{x_i x_j}\right\|} \frac{\Phi_f[x_j] - \Phi_f[x_i]}{\left\|\xi_{x_i x_j}\right\|^2} dA_{x_j} + R_f[x_i] \quad (32)$$

In the formula,

P_f represents the fluid density function, φ_f represents the ratio of fracture space volume to particle volume, Φ_f represents the water head of particles on the fracture surface, μ_f represents the fluid viscosity, k_f represents the fracture permeability, and R_f represents the source and sink terms of the fracture.

The uniform network discrete fracture seepage model was selected as the object, and the numerical analysis of the unit with a single fracture in the interior was verified by experimental verification under the action of a rapid stretching load.

As shown in Figure 4, a micro-element containing a single fracture is selected from the microscopic local area of a two-dimensional network's discrete fracture seepage model. The origin of the *xOy* coordinate system for this micro-element is the midpoint of the contained fracture. The *x* direction is horizontally 50 mm long, and the *y* direction is vertically 50 mm long. The vertical boundary is fixed, while the horizontal boundary is subjected to a tensile load, with no other fractures present inside. The horizontal length *L* of the micro-element is 50 mm, and the vertical length *W* is 50 mm. The initial fracture length 2*a* is 10 mm. Based on the common properties of coal seam surrounding rock, the elastic modulus is 30 GPa, Poisson's ratio is 0.33, and the density is 2400 kg/m^3. For the boundary conditions, the vertical boundary is fixed, and the horizontal boundary is subjected to a rapid tensile load in the form of displacement velocity, with v_y(x, ±L/2, t) being ±15 m/s and ±30 m/s, respectively. In terms of near-field dynamic discrete parameters, there are 500 material points in the *x* direction, 506 material points in the *y* direction (with 3 fixed points at the top and bottom of the vertical boundary), and 1 material point in the *z* direction. The material point spacing Δ is 1×10^{-4} m, the volume of a single material point ΔV is 1×10^{-12} m^3, and the volume of the virtual boundary layer, which is the volume of the fixed boundaries at the top and bottom, $\Delta V\delta$ is 3×10^{-10} m^3. The neighborhood range δ should be greater than 3Δ, and can be set to 3.014Δ. The critical elongation s_0 is 1 when there is no damage to the near-field interaction bonds between material points, and 0.04472 when damage is considered.

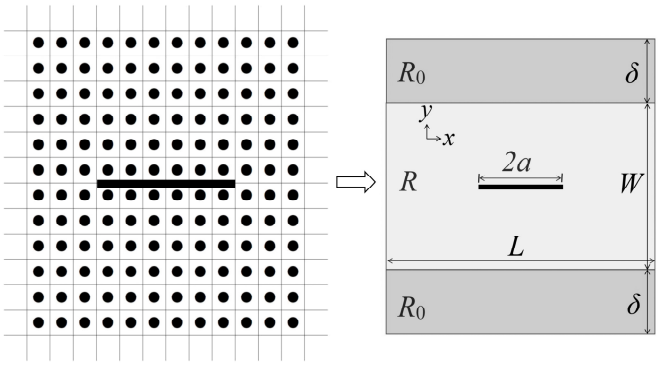
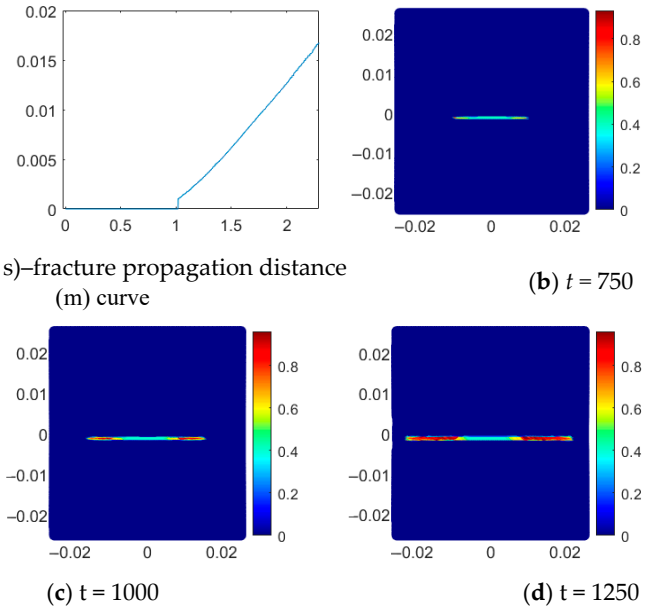


Figure 4. Schematic of calculation model of pore microunit in isotropic homogeneous medium.

In the numerical simulation, an adaptive dynamic relaxation method was not used, the critical elongation was considered for damage, the time step Δt was 1.33×10^{-8} s, and the total time step was 1250.

As shown in Figures 5 and 6, the trend of damage development can be observed under different synchronization and loading rates. When the velocity (v_y) is ±15 m/s, the

micro-element model shows self-similar crack propagation with a consistent expansion rate. However, when the velocity increases to ±30 m/s, the micro-element model exhibits bifurcated crack propagation, leading to fluctuations in the expansion rate. This model numerically simulates the different damage development processes of cracks under various loading conditions, yielding crack growth shapes that are more physically meaningful compared to traditional continuum mechanics.



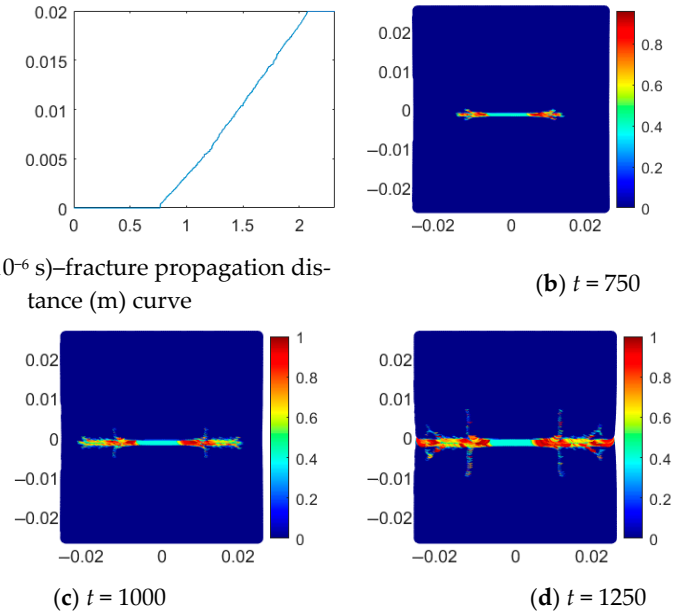
(**a**) Time (10^{-6} s)–fracture propagation distance (m) curve

(**b**) t = 750

(**c**) t = 1000

(**d**) t = 1250

Figure 5. Deformation results of micro-elements with fractures at different synchronous positions when v_y = ±15 m/s.



(**a**) Time (10^{-6} s)–fracture propagation distance (m) curve

(**b**) t = 750

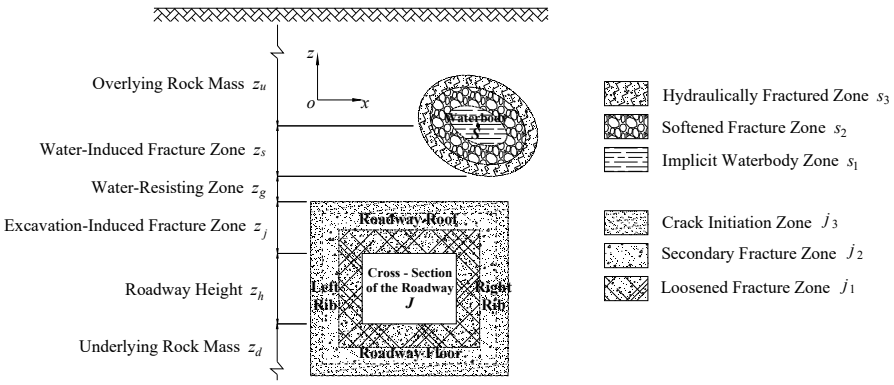
(**c**) t = 1000

(**d**) t = 1250

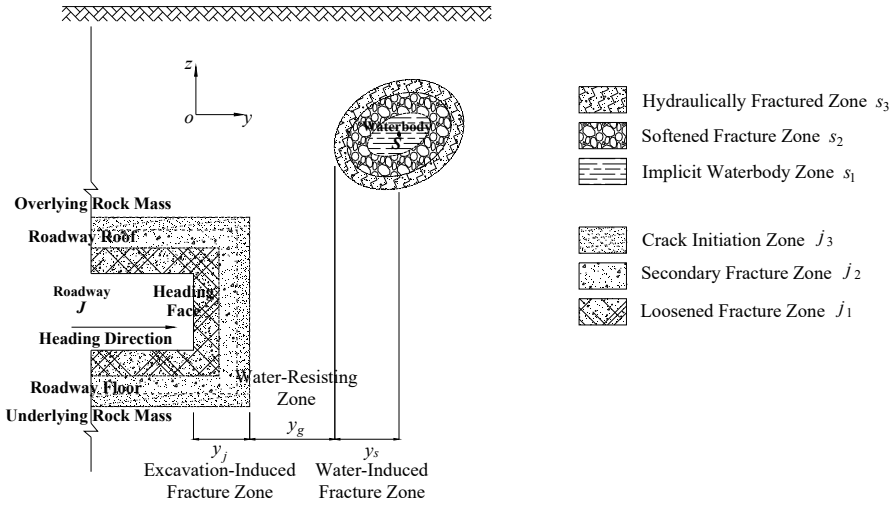
Figure 6. Deformation results of micro-elements with fractures at different synchronous positions when v_y = ±30 m/s.

2.4. Geometric Damage Dual-Control Model

Establish a "geometric damage" dual-control water inrush prediction model under the PD framework of the roadway shown in Figure 7. In front of the roof of roadway *J*, there is an implicit waterbody *S*. Assuming the distance between the roadway working face and the implicit waterbody is $D_{JS} = (y_{JS}, z_{JS})$, the formation of an effective water-conducting channel depends on whether the waterbody *S*'s water-induced fracture zone (y_s, z_s) and the roadway *J*'s excavation-induced fracture zone (y_j, z_j) can fully communicate, that is, whether the damage to the water-resisting zone (y_g, z_g) has reached a certain level.



(**a**) Direction of roadway section



(**b**) Direction of roadway excavation

Figure 7. "Geometric damage" dual-control water inrush prediction model for roadway.

(1) The evolution process of water-induced fracture zone

The evolution process is illustrated in Figure 8. The process begins with the presence of an implicit waterbody that exerts a certain level of pressure on the roof rock (s_1). This pressure weakens local solid bonds, leading to their fracture and the activation of fluid bonds, forming a softened fracture zone (s_2). Subsequently, this damage spreads and connects under the continued pressure of the water, ultimately forming a hydraulically fractured zone (s_3).

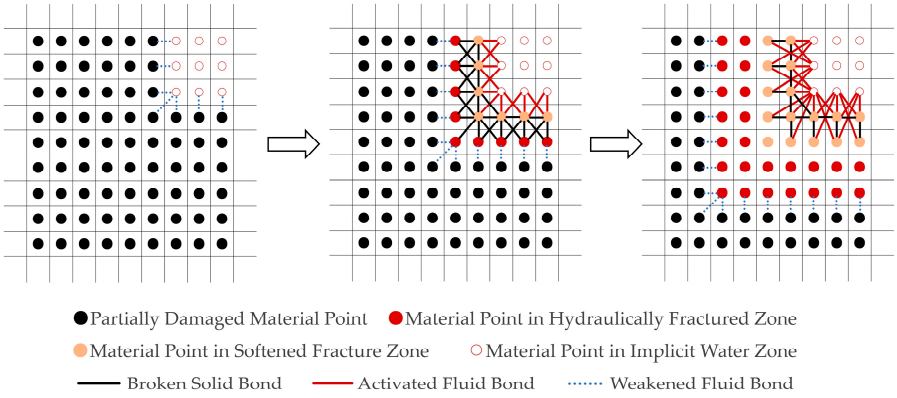


Figure 8. Schematic of the relationship between crack propagation and key fracture during the evolution of water-induced fracture zone.

(2) The evolution process of the excavation-induced fracture zone

The evolution process is illustrated in Figure 9. As the excavation progresses, the surrounding rock on the roof is affected by specific excavation techniques and engineering geological conditions: the integrity of the shallow surrounding rock around the roadway is compromised, leading to block separation (forming the loosened fracture zone j_1); the solid bonds of the middle surrounding rock around the roadway are broken, resulting in non-local stress failure (forming the secondary fracture zone j_2); the deep surrounding rock around the roadway experiences damage, with solid bonds breaking or weakening (forming the crack initiation zone j_3).

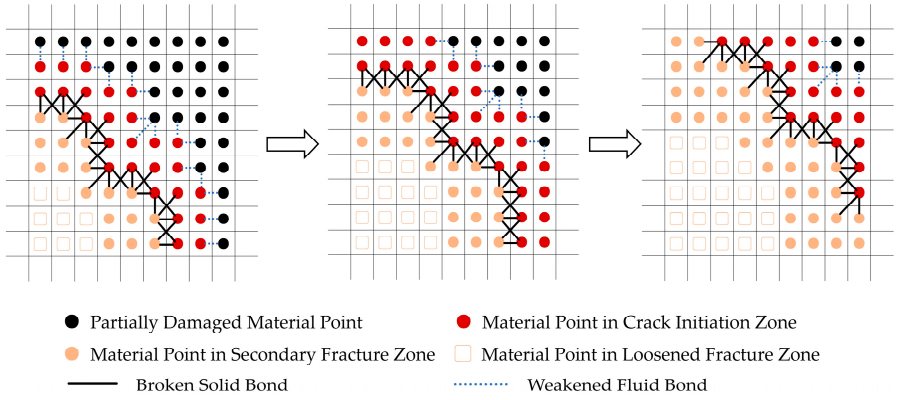


Figure 9. Schematic of the relationship between crack propagation and key fracture during the evolution of excavation-induced fracture zone.

(3) The destruction of the water-resisting zone and the effectiveness of the conduction

As shown in Figure 10, the destruction process of the water-resisting zone can be divided into three levels: completely undamaged, partially damaged, and completely destroyed.

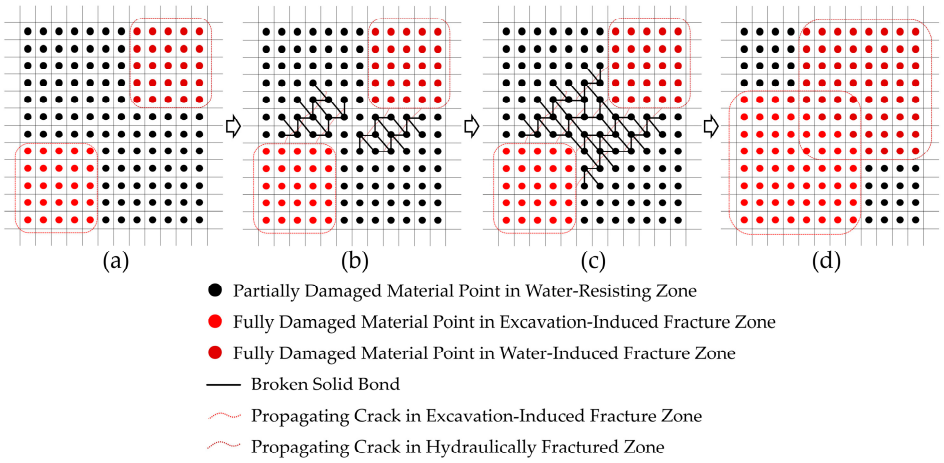


Figure 10. Schematic of the relationship between crack propagation and key fracture during the destruction of water-resisting zone.

(1) The water-resisting zone is completely undamaged ($y_g > 0$ and $z_g > 0$):

As shown in Figure 10a, all solid bonds in the water-resisting zone are intact → local damage, as determined by Equation (14) (i.e., the ratio of the number of broken bonds to the total number of bonds), $D_{aquiculude}$ $(y,t) = 0$ and $D_{aquiculude}$ $(z,t) = 0$ → the water-conducting channel has not yet formed → it can be considered that water will not occur suddenly.

(2) Part of the water-resisting zone is damaged ($y_g \cdot z_g \leq 0$):

As shown in Figure 10b, the partial fracture of the solid bond in the water-resisting zone has caused local damage that has not reached the critical condition. Specifically, if $0 < D_{aquiculude}(y,t) < D_{critical}$ and $0 < D_{aquiculude}(z,t) < D_{critical}$, the current drainage channel is not fully formed, leading to insufficient effectiveness. Therefore, it can be concluded that a sudden water surge is unlikely to occur at this time, although the possibility of a delayed-type sudden water surge cannot be ruled out.

As shown in Figure 10c, when most of the solid bonds in the water-resisting zone break, causing local damage to reach the critical condition, it is concluded that the local damage $D_{critical} \leq D_{aquiculude}(y,t) < 1$ or $D_{critical} \leq D_{aquiculude}(z,t) < 1$. This indicates that the water-conducting channel has initially formed and is highly effective, suggesting that either a lag-type sudden water inrush or an instantaneous sudden water inrush may occur.

(3) The water-resisting zone was completely destroyed ($y_g < 0$ and $z_g < 0$):

As shown in Figure 10d, all the solid bonds in the water-resisting zone are broken, and the water conduction channel has been formed and is fully effective. When $D_{critical} \leq D_{aquiculude}(y,t) \leq 1$ and $D_{critical} \leq D_{aquiculude}(z,t) \leq 1$, it can be considered that instantaneous water inrush will occur.

2.5. Unified Single-Exponential Discriminant Function (T_{JS})

Existing scholars have conducted certain research on the prediction of water hazards in roadways, but they have not yet performed dual analysis and prediction from both geometric space and rock mass damage perspectives simultaneously [17–24]. In the "geometric damage" dual-control water inrush prediction model under the PD framework for tunneling, the distance between the working face and the concealed water is denoted as D_{JS}. If a water-probing borehole at the face of the excavation detects the boundary of the concealed water, with the depth of the borehole being L_T and the angle to the horizontal

plane being β_T, then the distance between the face of the excavation and the concealed water can be expressed as

$$\begin{cases} y_{JS} = L_T \cos \beta_T \\ z_{JS} = L_T \sin \beta_T \end{cases} \tag{33}$$

Whether the water diversion channel is completely open can be given by the condition that the water-resisting zone (y_g, z_g) is completely destroyed:

$$\begin{cases} y_g < 0 \\ z_g < 0 \end{cases} \tag{34}$$

The range of the water-resisting zone can be obtained by subtracting the distance between the head of the excavation face and the implicit waterbody from the water-induced fracture zone and the excavation-induced fracture zone:

$$\begin{cases} y_g = y_{JS} - y_s - y_j \\ z_g = z_{JS} - z_s - z_j \end{cases} \tag{35}$$

When the water channel of Equation (34) is fully open, it can be expressed as

$$\begin{cases} y_{JS} - y_s - y_j < 0 \\ z_{JS} - z_s - z_j < 0 \end{cases} \tag{36}$$

The above formula is the basic discriminant of the complete effectiveness of the water conduction channel. A unified discriminant function for the effectiveness of the water diversion channel on the roof of roadway excavation is constructed:

$$T_{JS} = \sqrt{e}^{\frac{y_s + y_j}{y_{JS}} - 1} \cdot \sqrt{e}^{\frac{z_s + z_j}{z_{JS}} - 1} + \sqrt{\kappa}^{1 - \mathrm{sign}(y_s + y_j - y_{JS}) \cdot sign(z_s + z_j - z_{JS})} \tag{37}$$

In the formula, T_{JS} is the effective coefficient of the water conduction channel in roadway excavation, where $T_{JS} > 0$, and κ is the critical value of peridynamics local damage related to $D_{aquiculude}$, $0 < \kappa < 1$, approximated by the porosity of coal–rock mass in the absence of local damage.

The effectiveness judgment function and principles for the water conduction channel in the roadway roof are detailed in Table 1. Based on these principles, during the roadway excavation process, the effective coefficient T_{JS} of the water diversion channel can be calculated by selecting appropriate basic parameters based on actual conditions, allowing for the assessment of the water diversion channel's effectiveness.

Table 1. Effectiveness discrimination function and discrimination principle of water conduction channel in roadway roof.

Concrete Circumstances	Corresponding Conditions	Form of Effective Judgment Function of Water Diversion Channel	Principle of Effective Judgment of Water Conduction Channel
The water-resisting zone was completely undamaged	$y_g > 0$ $z_g > 0$	$T_{JS} = \sqrt{e}^{(\frac{y_s + y_j}{y_{JS}} - 1)(\frac{z_s + z_j}{z_{JS}} - 1)}$	$T_{JS} < 1$. The closer T_{JS} is to 0, the safer it is, and the water conduction channel is invalid, so it can be considered that there will be no sudden water inrush.

Table 1. *Cont.*

Concrete Circumstances	Corresponding Conditions	Form of Effective Judgment Function of Water Diversion Channel	Principle of Effective Judgment of Water Conduction Channel
Parts of the water-resisting zone were damaged	$y_g < 0$ $z_g > 0$	$T_{JS} = \sqrt{e^{(\frac{y_s+y_j}{y_{JS}}-1)(\frac{z_s+z_j}{z_{JS}}-1)}} + \kappa$	$T_{JS} < 1$: The closer T_{JS} is to 0, the lower the effectiveness of the water conduction channel; it can be considered that the sudden water will not occur temporarily, but there is the possibility that lagging-type sudden water cannot be ruled out; the closer T_{JS} is to 1, the higher the effectiveness of the water conduction channel. It can be considered that the lagging-type sudden water or instantaneous-type sudden water may occur. When $T_{JS} > 1$, the water conduction channel is highly effective, and instantaneous water inrush may occur. When $T_{JS} > 1 + \kappa(y_g \cdot z_g < 0)$ or $1 + \sqrt{\kappa}$ $(y_g \cdot z_g = 0)$, the water conduction channel is effective, and instantaneous water inrush can be considered to occur.
	$Y_g < 0$ $z_g = 0$	$T_{JS} = \sqrt{e^{\frac{y_s+y_j}{y_{JS}}-1}} + \sqrt{\kappa}$	
	$y_g = 0$ $z_g = 0$	$T_{JS} = 1 + \sqrt{\kappa}$	
	$y_g = 0$ $z_g < 0$	$T_{JS} = \sqrt{e^{\frac{z_s+z_j}{z_{JS}}-1}} + \sqrt{\kappa}$	
	$y_g > 0$ $z_g < 0$	$T_{JS} = \sqrt{e^{(\frac{y_s+y_j}{y_{JS}}-1)(\frac{z_s+z_j}{z_{JS}}-1)}} + \kappa$	
The water-resisting zone was completely destroyed	$y_g < 0$ $z_g < 0$	$T_{JS} = \sqrt{e^{(\frac{y_s+y_j}{y_{JS}}-1)(\frac{z_s+z_j}{z_{JS}}-1)}}$	When $T_{JS} > 1$, the larger the T_{JS}, the more dangerous it is. The water conduction channel is effective, and instantaneous water inrush can be considered to occur.

2.6. Coal Mine Roadway Water Inrush Prediction and Assessment Procedure

Building upon the theoretical foundation, Figure 11 presents the coal mine water inrush prediction and assessment flowchart for excavation roadway roofs, structured in three consecutive modules.

(1) Water-induced fracture zone quantification

Site-specific rock mechanics parameterization assesses hydraulic overpressure conditions to analyze and compute the hydraulically fractured zone's extent. Chemically degraded parameters define the softened fracture zone boundaries, ultimately delineating the water-induced fracture zone.

(2) Excavation-induced fracture zone quantification

The transient energy shock characteristics were verified through excavation methods. In mechanized excavation without transient energy, a fracture zone can be calculated via roadway parameters and geomechanical properties. In drilling–blasting excavation with blast-induced transient energy shock, extents of loosened, secondary, and crack initiation zones are analyzed and quantified using blasting and rock mass parameters.

(3) Prediction evaluation and refinement loop

The water-resisting zone extent is determined based on working face advance water detection data. Peridynamics local damage modeling computes the stability coefficient T_{JS}, establishes discriminant criteria for prediction evaluation, and terminates or refines the process per validity assessment.

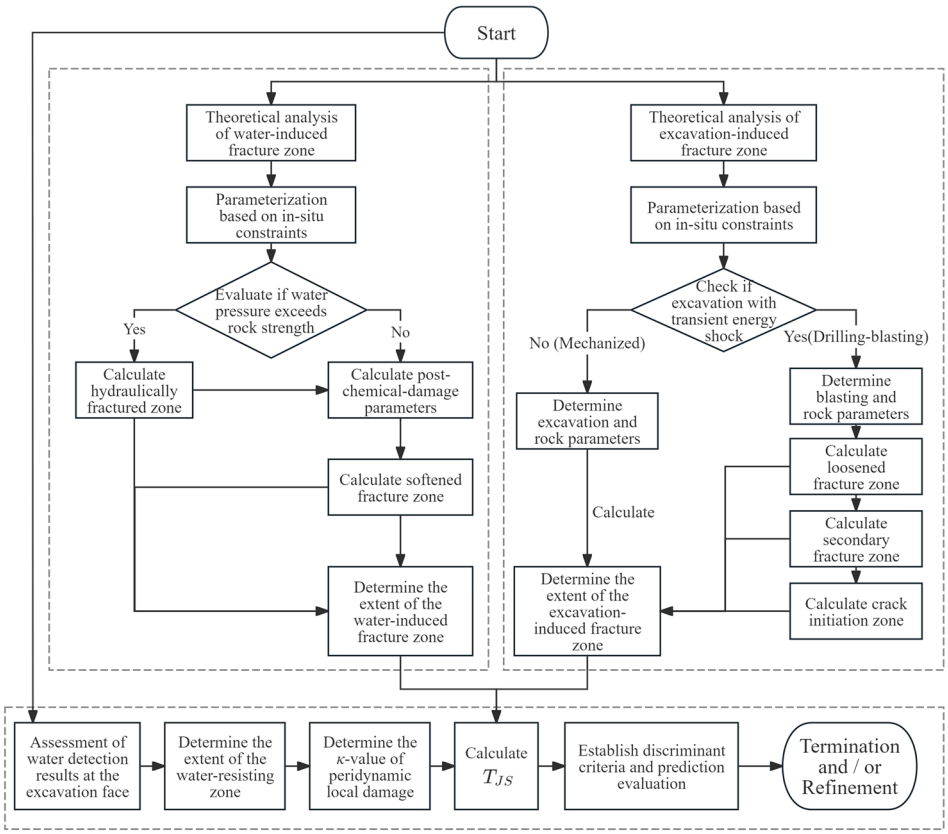


Figure 11. Flowchart for water inrush prediction in excavation roadway roofs.

3. Results

3.1. Cases 1: Prediction and Assessment of Water Inrush During Mechanized Excavation at Yishun Coalmine

3.1.1. Case Overview

On 24 October 2016, before the excavation of roadway No.9103 at Yishun coalmine in Pinglu District, Shuozhou City, Shanxi Province, China, a transient electromagnetic instrument was used to conduct preliminary geophysical exploration. The exploration results indicated a low-resistance anomaly 60–120 m ahead of the roadway, requiring drilling verification. In fact, above the water inrush point of roadway No.9103, there is a north–south ventilation alley that was excavated in 2008 along the roof of the No.9 coal seam, as shown in Figure 12. This area has extensive ancient water.

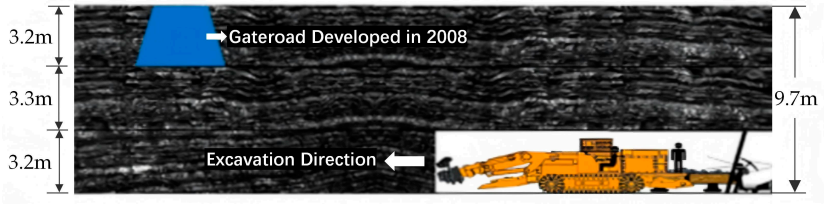


Figure 12. Schematic of accident area of roadway No.9103.

On 2 November 2016, during the excavation of roadway No.9103, a water surge occurred when the roadway passed beneath an old roadway without taking water probing and drainage measures. The water volume was approximately 8000 m^3, resulting in two deaths, two injuries, and direct economic losses of CNY 70.4 million. This incident was classified as a non-tectonic control type, with the water surge being instantaneous. The

roadway was excavated using a comprehensive excavation method, and the direct water source was old mine water.

3.1.2. Quantification of Water-Induced Fracture Zone

In the "geometry injury" dual-control water inrush prediction model, the water-induced fracture zone (y_s, z_s) is composed of implicit waterbody zone s_1, softened fracture zone s_2, and hydraulically fractured zone s_3. The water pressure gradient is Δp. According to Darcy's law [10,13], the expression form of the water pressure gradient can be obtained:

$$\Delta p = \frac{Q \cdot L}{A \cdot K} \tag{38}$$

In the formula, Q represents the minimum volume flow of fracture conductivity, L represents the length of fracture, A represents the area of the fracture opening cross-section, and K represents the permeability coefficient of coal–rock mass.

If the equivalent hydraulic opening of a coal–rock mass fracture is equal to the equivalent radius of the fracture opening cross-section, b, it is substituted into the calculation of the fracture opening-cross section area:

$$\Delta p = \frac{Q \cdot L}{\pi b^2 \cdot K} \tag{39}$$

If the inclination angle of the coal-bearing stratum to the horizontal plane is β_1 and the inclination angle of the main joint to the coal-bearing stratum is β_2, the range of hydraulically fractured zone s_3 can be obtained:

$$\begin{cases} s_{3z} = \max\left\{\cos\beta_1 \cos\beta_2 \cdot L_z, \quad \sin\beta_1 \sin\beta_2 \cdot L_y\right\} \\ s_{3y} = \max\left\{sin\beta_1 \sin\beta_2 \cdot L_z, \quad cos\beta_1 \cos\beta_2 \cdot L_y\right\} \end{cases} \tag{40}$$

It is assumed that after the water chemical damage, the cohesion and internal friction angle of the coal mass decrease to a certain proportion compared with that before the damage, respectively:

$$C' = C(1 - S_c/100) \tag{41}$$

$$\varphi' = \varphi(1 - S_\varphi/100) \tag{42}$$

In the formula, C' represents the cohesion after hydrochemical damage, S_C represents the percentage coefficient of cohesion reduction, φ' represents the internal friction angle after hydrochemical damage, and S_φ represents the percentage coefficient of internal friction angle reduction.

To determine the values of S_C and S_φ, coal–rock samples (sandstone) from roadway No.9103's working face were immersed in a solution with a pH value of 5. Peak shear strength tests were conducted at different soaking times (t = 7 d, 30 d, 60 d, 90 d, 120 d). Regression analysis was performed on the measured cohesion and internal friction angle to obtain a goodness of fit > 0.95. The expressions for the changes in S_C and S_φ over time are as follows:

$$S_c = 6.45\ln(t + 11.59) - 12.56 \tag{43}$$

$$S_\varphi = 0.0912t^{0.76} + 1.15 \tag{44}$$

Since the water chemical damage occurs mainly on the contact surface, the range of softened fracture zone s_2 can be obtained:

$$\begin{cases} s_{2z} = K\pi b^2 \cdot (p - C' - \sigma_z \cdot \tan\varphi')/Q \\ s_{2y} = K\pi b^2 \cdot (p - C' - \lambda\sigma_z \cdot \tan\varphi')/Q \end{cases} \quad (45)$$

Then, the geometric expression of the water-induced fracture zone can be expressed as follows:

$$\begin{cases} y_s = s_{2y} + s_{3y} \\ z_s = s_{2z} + s_{3z} \end{cases} \quad (46)$$

The soaking time of water in the working face of roadway No.9103 was gradually adjusted from 0 d to 2560 d, and the range of the water-induced fracture area under different soaking times was calculated, as shown in Table 2. It was drawn into an influence curve, as shown in Figure 13.

Table 2. Influence of soaking time on the range of the fissure zone in water.

Soak Period (d)	y_s (m)	z_s (m)	Soak Period (d)	y_s (m)	z_s (m)
15	0.110	0	360	2.203	1.483
30	0.458	0.062	480	2.437	1.732
60	0.883	0.115	960	3.024	2.375
120	1.364	0.607	1440	3.389	2.788
180	1.664	0.918	1920	3.661	3.105
240	1.884	1.147	2560	3.945	3.444

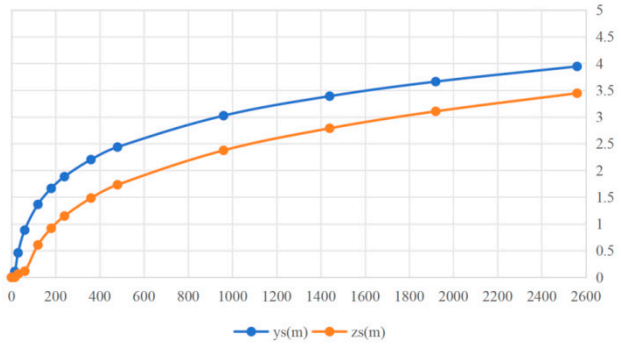


Figure 13. Curve of influence of soaking time on the range of the fissure zone in water.

The development of water-induced fracture zones in the working face is primarily influenced by the hydrochemical effects of accumulated water, leading to a decline in the physical and mechanical properties of the surrounding rock, with the soaking-softened fracture zone being predominant. As shown in Figure 13 and Table 2, the extent of the softened fracture zone increases with the duration of soaking. Compared to damage along the strike direction, vertical damage develops more slowly and is less severe, but both show a similar growth trend. The growth rate is higher between 0 and 240 days, gradually slows down from 240 to 1440 days, and then stabilizes after 1440 days, indicating that the hydrochemical damage effect decreases over time.

3.1.3. Quantification of Excavation-Induced Fracture Zone

The excavation-induced fracture zone (y_j, z_j) is composed of loosened fracture zone j_1, secondary fracture zone j_2, and crack initiation zone j_3. The excavation failure range is

obtained through the mechanical analysis of the circular standardization of a non-circular roadway, and the following formula is obtained [25,26]:

$$a = \min\left\{k_x\left(\frac{S}{\pi}\right)^{1/2}, \left(r_c{}^2 + h_c{}^2\right)^{1/2}\right\} \tag{47}$$

In the formula,

a represents the theoretical radius of the roadway, S represents the actual cross-sectional area of the roadway, h_c represents the height of the straight wall section, r_c represents the radius of the arch section (half of the width of the rectangular roadway), and k_x represents the correction coefficient of the roadway section, which is 1.1~1.3.

The surrounding rock is mainly subjected to shear failure, and the radius of loosened fracture zone j_1 and secondary fracture zone j_2 is as follows:

$$R_a = a\left[\frac{(P + C\cot\varphi)(1 - \sin\varphi)}{C\cot\varphi}\right]^{\frac{1-\sin\varphi}{2\sin\varphi}} \tag{48}$$

In the formula, P represents the stress of the original rock, C represents the cohesion of the roof surrounding rock, and φ represents the internal friction angle of the roof surrounding rock.

In the evolution analysis model of the water conduction channel on the roof of the roadway excavation, the starting point of the fracture zone in the roadway excavation is at the geometric center of the head of the roadway excavation, and the geometric expression is as follows:

$$\begin{cases} y_j = R_a \\ z_j = R_a + r_c \end{cases} \tag{49}$$

In the formula, R_a is the radius of the loosened fracture zone and the secondary fracture zone determined by Formula (48), and r_c represents the radius of the arch section (half of the roadway width for a rectangular roadway).

It is noted that when the section form of the roadway is a rectangular section with a high span ratio less than 1, which is common in coal roadways, the range expression of the excavation fracture zone can be obtained:

$$\begin{cases} y_j = k_x\left(\frac{d_c h_c}{\pi}\right)^{1/2} \cdot \left[\frac{(P+C\cot\varphi)(1-\sin\varphi)}{C\cot\varphi}\right]^{\frac{1-\sin\varphi}{2\sin\varphi}} \\ z_j = k_x\left(\frac{d_c h_c}{\pi}\right)^{1/2} \cdot \left[\frac{(P+C\cot\varphi)(1-\sin\varphi)}{C\cot\varphi}\right]^{\frac{1-\sin\varphi}{2\sin\varphi}} + \frac{d_c}{2} \end{cases} \tag{50}$$

In the formula, d_c represents the roadway width.

The section form of roadway No.9103 is a common rectangular section in a coal roadway, with a high span ratio of 0.8. The comprehensive mechanized excavation method was adopted, and there was no instantaneous violent energy dynamic impact. The final calculation results of the excavation-induced fracture area are y_j = 1.496 m and z_j = 3.496 m.

3.1.4. Prediction Evaluation of Single-Exponential T_{JS} Index

The prediction and evaluation period spans from 24 October, when the geological survey detected a low-resistance anomaly 60 to 120 m ahead of roadway No.9103's working face, to 2 November, when an accident occurred. Over this 9-day period, a total of 53 m was excavated, averaging about 6 m per day. T_{JS} was calculated based on the excavation progress during this period, and the resulting T_{JS} curve is illustrated in Figure 14.

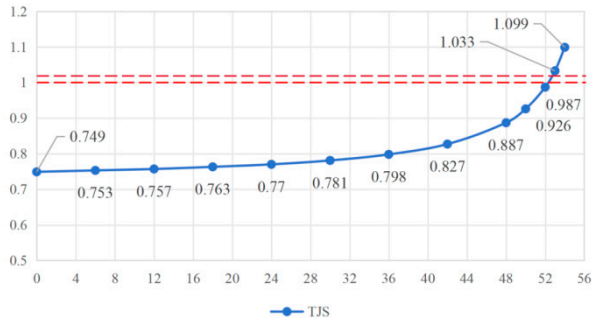


Figure 14. T_{JS} curve of excavation progress from October 24 to November 2 of roadway No.9103.

According to the principle of evaluating the effectiveness of water conduction channels in the roof of roadway excavation, when the roadway began excavation, T_{JS} was 0.749, which is close to 1, indicating that the water conduction channel has a certain level of effectiveness. As the excavation depth increases, T_{JS} shows an increasing trend, with its curve slope becoming steeper and its value approaching 1, indicating higher water conduction channel effectiveness. After the excavation reaches 40 m, if T_{JS} exceeds 0.8, there is a high likelihood of delayed or instantaneous water inrush, especially after reaching 49 m, where T_{JS} exceeds 0.9, significantly increasing the risk of instantaneous water inrush.

As the roadway excavation depth increased, the T_{JS} growth rate accelerated. Between 1 November and 2 November, it surpassed the first critical threshold line $T_{JS} = 1$. On the night shift of 2 November, when the excavation reached 53 m, T_{JS} reached 1.033, exceeding the second critical threshold line $T_{JS} = 1 + \kappa$. This indicates that the water diversion channel was fully effective, and an instantaneous water inrush was likely to occur. According to the accident investigation, at 22:45 on 1 November 2016, the personnel of the second excavation team entered the shaft for work. About one hour later, the team leader started the excavation machine. After excavating about 2 m, a sudden water inrush occurred. The accident occurred at 03:46 on 2 November 2016, with the excavation depth reaching 53 m. The analysis confirms that the timing of the accident and the excavation depth are consistent with the research findings.

3.2. Cases 2: Prediction and Assessment of Water Inrush During Drilling–Blasting Excavation with Transient Energy Shock at Zhongcun Coalmine

3.2.1. Cases Overview

On 27 January 2023, during roadway excavation along the No.3 coal seam floor at the ZF1212 heading face of Jushan coalmine (Shanxi Lanhua Group, Jincheng City), unidentified water accumulation from overlying abandoned workings breached the coal face due to unmitigated hazards. Approximately 7100 m^3 of water inundated the excavation zone, resulting in four fatalities and direct economic losses of CNY 8.7612 million. This accident is categorized as a structurally uncontrolled instantaneous water inrush, occurring in a drilling–blasting excavation roadway.

The accident occurred at the heading face of ZF1212 roadway in Panel 1 of the No.3 coal seam, located 117 m from the portal. Geometrical configurations include a coal seam strike angle of +11°, rectangular cross-section (width 3.4 m; height 2.5 m), and daily advance rate of 3 m. Prior to the accident, the primary mining scope encompassed the northern wing of Panel 1 in the No.3 coal seam, exclusively involving secondary mining operations with localized abandoned goaf areas remaining from historical No.3 seam extraction. The ZF1212 excavation roadway was situated within this northern wing, where the No.3 seam averaged 4.2–6.12 m thickness. Numerous goaf areas had formed due to room-and-pillar mining conducted along the roof. Excavation at 90 m encountered a steep strata dip rise that exposed sandy mudstone flooring. This resulted in persistent half-coal–rock conditions

up to the 117 m incident location. The operational design required anomaly detection ahead via transient electromagnetic (TEM) prospecting and underground borehole probing (long-range/short-range). Ultimately, both methods failed to identify the water hazard ahead.

In the TEM survey on 2 January at 70 m, 100 m coverage failed to consider significant strata attitude changes near the synclinal axis. No design adjustment corrected the undetected transition from bedding-parallel to floor-perpendicular detection. This caused critical omission at 117 m.

For drilling operations after reaching 112 m, the final long-range probing on 19 January executed only four boreholes during 8:00/16:00 shifts versus the eight designed. All holes measured <20 m against the required >30 m depth. Furthermore, short-range probing was omitted for six consecutive shifts pre-accident.

3.2.2. Quantification of Water-Induced Fracture Zone

The geomechanical properties of the ZF1212 excavation roadway surrounding rock comprise a cohesion of 2.1 MPa, friction angle of 32°, Poisson's ratio of 0.33, tensile strength of 0.53 MPa, permeability coefficient of 17.66 m/d, and porosity of 6%, with an overburden depth of 0.136 km and average rock density of 17 kN/m^3. The concealed water body ahead exhibits water pressure of 0.19 MPa at pH 7 after 6000-day saturation. Based on the aforementioned parameters and referencing the analytical methodology in Section 3.1.2, the final calculated extents of the water-induced fracture zone for the ZF1212 excavation roadway are y_s =2.548 m and z_s =2.544 m.

3.2.3. Quantification of Excavation-Induced Fracture Zone

The ZF1212 excavation roadway adopted drilling–blasting excavation. This method generates blast-induced transient energy shock during detonation, significantly expanding the surrounding rock damage scope [27].

Under instantaneous intense dynamic impact loading from blasting, surrounding rock primarily experiences compressive and tensile failure. The damage zones radiate outward sequentially, forming a loosened fracture zone (j_1), a secondary fracture zone (j_2), and a crack initiation zone (j_3). Blasting excavation charge configurations are categorized as either coupled charges or decoupled charges. Different charging methods induce distinct loading patterns on borehole walls, resulting in varying degrees of rock damage.

Within the loosened fracture zone, coal–rock masses exhibit severe fragmentation with extensively interconnected fractures. The dominant failure mechanism under blasting is tensile failure under plane stress conditions [28]. The influence of excavation-induced hoop stresses is negligible here; only radial effects are considered. This failure mode satisfies the Drucker–Prager criterion under pure tensile conditions. Based on the radial stress expression derived from tensile failure under the Drucker–Prager criterion during blasting shockwave propagation, the radius Rj_1 of zone j_1 is expressed as

$$R_{j_1} = r_b \left[\frac{P(1-\sin\varphi)}{2c\cos\varphi} \right]^{\frac{1}{a}} \tag{51}$$

In the formula, P represents the shockwave pressure, C represents the cohesion of the roof surrounding rock, φ represents the internal friction angle of the roof surrounding rock, a represents the stress wave attenuation index, and r_b represents the borehole radius.

The secondary fracture zone contains numerous relatively wide fractures with limited propagation and connectivity [29]. Coal–rock masses in this zone experience combined tensile and compressive stresses. The boundary between zones j_2 and j_3 corresponds to the

critical position where the rock mass loses its hoop-bearing capacity. By establishing the hoop stress equilibrium equation at this interface, the radius Rj_2 of zone j_2 is derived as

$$R_{j_2} = r_b \left(\frac{\lambda P}{\sigma_b} \right)^{\frac{1}{a}} \tag{52}$$

In the formula, λ represents the lateral pressure coefficient, and σ_b represents the tensile strength of the coal–rock mass.

When fractures in zone j_2 propagate into the crack initiation zone (j_3), the radius R_{j_3} of zone j_3 is determined through the simultaneous solution and simplification of the critical stress intensity factor at crack tips [30], and the impact forces generated by blasting gases filling zone j_1. This yields the expression

$$R_{j_3} = R_{j_2} \left[\frac{2(1+\gamma){R_{j_1}}^2}{r_b(r_b+r_c)\rho_B D^2} \cdot \frac{P}{F} \right]^2 \cdot \left(\frac{R_{j_2}}{r_b} \right)^{-2a} \tag{53}$$

In the formula, γ represents the adiabatic exponent of detonation product expansion, r_c represents the charge radius (where r_b/r_c constitutes the radial decoupling coefficient of the charge), F represents the fracture length coefficient, ρ_B represents the explosive density, and D represents the detonation velocity of the explosive.

The radii of blast-induced fracture zones were calculated under varying decoupling coefficients: R_{j1} (loosened fracture zone), R_{j2} (secondary fracture zone), and R_{j3} (crack initiation zone), with total radius $\sum R_{ji}$ (combined excavation-induced fracture zone). The results are compiled in Table 3. At a decoupling coefficient of 1.25, the final calculated extents are y_j =7.052 m and z_j = 7.074 m. Notably, the crack initiation zone radius R_{j3} constitutes over 57% of the total blast-induced fracture radius $\sum R_{ji}$.

Table 3. Calculated radii of blast-induced fracture zones under varying decoupling coefficients for the ZF1212 roadway.

Decoupling Coefficients	R_{j1} (m)	R_{j2} (m)	R_{j3} (m)	$\sum R_{ji}$ (m)
1	3.819	2.919	195.334	1
1.1	2.694	2.059	37.484	1.1
1.2	1.958	1.497	8.242	1.2
1.3	1.463	1.119	2.063	1.3
1.4	1.116	0.853	0.567	1.4
1.5	0.867	0.663	0.170	1.5
1.6	0.685	0.524	0.055	1.6
1.7	0.549	0.420	0.019	1.7
1.8	0.445	0.340	0.007	1.8
1.9	0.365	0.279	0.003	1.9
2	0.303	0.232	0.001	2

3.2.4. Prediction Evaluation of Single-Exponential T_{JS} Index

The prediction and evaluation commenced at the slope change point located 90 m into the excavation face of heading ZF1212 on 10 January and concluded at the 117 m mark where the incident occurred on 26 January, encompassing a total advance of 27 m. Throughout this excavation segment, no geophysical exploration was conducted. Based on the drilling design and its implementation, calculations were performed using a long drilling advance distance of 30 m and a dip angle of 5.74°. The results of these calculations are presented graphically as a curve of the excavation progress versus T_{JS}, as illustrated in Figure 15.

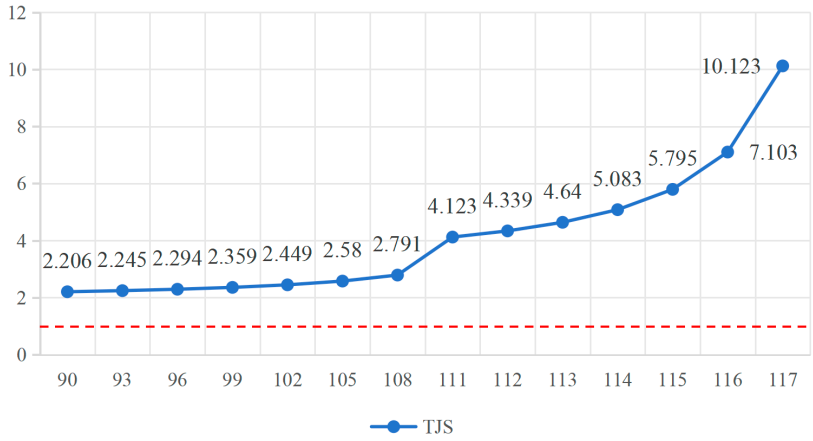


Figure 15. T_{JS} curve of excavation progress from 10 January to 26 January of roadway ZF1212.

Throughout the blast excavation from the 90 m to 117 m mark in the ZF1212 heading face, T_{JS} consistently remained above the discriminant threshold line, indicating persistently high potential for water inrush. As calculated, conditions $z_g < 0$ and $y_g > 0$ were observed during excavation between 90 m and 108 m, signifying that hydraulic connectivity between the water-induced fractures and excavation-induced fractures had been established in the vertical direction. Furthermore, the extent of fracture propagation in the vertical dimension critically compromised the integrity of the water-resisting zone. Beyond the 108 m advance point, conditions $z_g < 0$ and $y_g < 0$ were calculated, accompanied by an abrupt change in the T_{JS} curve. This demonstrates that effective hydraulic pathways had become fully developed, suggesting imminent instantaneous water inrush. The predictive results indicate that the ZF1212 heading face advanced under continuously hazardous conditions with imminent water inrush risk from the 90 m slope-change point onward.

4. Discussion

4.1. Parameter Sensitivity Analysis

The critical damage threshold κ emerges as the most sensitive parameter in the dual-control prediction model. Conducted via Python 3.7 [31–34], Monte Carlo simulation (n = 10,000) revealed the existence of underestimation risk and overestimation tendency. When $\kappa < 0.3$, false negative rates increase to 38.7% for delayed water inrush ($T_{JS} > 0.8$) due to premature channel effectiveness assessment. At $\kappa > 0.7$, false alarms rise by 22.4% for instantaneous inrush prediction ($\$T_{JS} > 1 + \kappa$). When $\kappa = 0.45 \pm 0.05$, optimal calibration achieves 91.3% accuracy in the Yishun case (Figure 14), aligning with the porosity of surrounding rock mass (0.43–0.48) in the water-resisting zone. The κ-value physically represents the percolation threshold where broken solid bonds form connected pathways. This mechanistic insight explains its dependence on lithology.

4.2. Comparative Study with Classical Methods

PD-based dual-control model demonstrates significant improvements versus existing approaches, as shown in Table 4.

PD dual-control model would have triggered alerts at $T_{JS} = 0.82$(Day 7) during the Yishun accident precursor period (24 October–1 November) and remained on alert during the Zhongcun accident precursor period (10 January–26 January), while Sun et al.'s empirical method [35] issued no warning ($R < 0.6$) and Qiao's separation layer model [36] produced false negatives until the final hour.

Table 4. Influence of soaking time on the range of the fissure zone in water.

Model Type	Prediction Accuracy	Real-Time Applicability	Key Limitation
Empirical formulas [13,17]	62.3 ± 8.7%	Low (requires manual measurement)	Ignores damage evolution
FEM simulations [19,22]	74.1 ± 6.2%	Very low (hours per simulation)	Continuum assumption fails at fractures
PD dual-control (Ours)	91.8 ± 3.5%	High (T_{JS} updates in minutes)	Requires κ calibration

4.3. Limitations and Uncertainty

Three critical limitations warrant attention. First, detection error propagation occurs when the borehole deviation exceeds 10°, causing a 15–30% error in D_{JS}. Second, under high-velocity flow regimes where the Reynolds number (R_e) exceeds 2300, the Navier–Stokes simplification (Equation (25)) underestimates the flow by 18–27%. Third, the current model does not fully account for damage anisotropy in rock masses, as field data indicate fracture growth rates 40% higher along bedding planes. Future model refinements should incorporate orientation-dependent bond-breaking criteria.

4.4. Practical Implications

Building upon the T_{JS} threshold system established in this study, a staged prevention strategy for mine water inrush hazards can be developed. This strategy implements dynamic responses wherein safe operations are maintained when $T_{JS} \leq 0.8$. If T_{JS} exceeds 0.8, a Stage-1 Alert is triggered with enhanced borehole probing frequency. Upon T_{JS} surpassing 0.9, the procedure escalates to Stage-2 Evacuation, mandating immediate withdrawal if $T_{JS} \geq 1 + \kappa$ or initiating drainage system preparation otherwise. This tiered mechanism synergistically optimizes preemptive disaster mitigation and operational sustainability.

5. Conclusions

5.1. Restated Objective

Local damage criteria of peridynamics types are established, a "geometry damage" dual-control water inrush prediction model is established, the evolution law of the water-induced fractures zone and excavation-induced fractures zone is quantitatively analyzed, the concept of a critical damage threshold in the water-resisting zone is proposed, and the essential difference between lagging-type sudden water and instantaneous-type sudden water is explained. The rationality of the method is verified through different typical case studies of roof water inrush accidents in roadways, providing theoretical and practical significance for water inrush prediction and advanced prevention in the excavation of coal mine roadways.

5.2. Key Findings

The constructed unified discriminant function effectively integrates geometric parameters and damage variables and combines the damage critical value to form a single index prediction and evaluation system that realizes the dynamic quantitative evaluation of the effectiveness of the water conduction channel.

When T_{JS} exceeds 0.8, the risk of lagging sudden water inrush increases significantly; when $T_{JS} \geq 1 + \kappa$, the instantaneous sudden water inrush can be accurately predicted, which is highly consistent with the accident advance and excavation time, verifying the feasibility and rationality of the prediction model.

5.3. Future Work

The next phase will pursue three interconnected advancements: implementing machine learning-driven dynamic calibration for the proposed water inrush prediction coefficient, extending the peridynamics water inrush model into three-dimensional simulations for excavation roadways, and developing a dedicated T_{JS} monitoring and staged prevention system for mining applications. Collectively, these initiatives will establish an intelligent closed-loop framework for real-time water inrush risk early warning during underground excavation.

Author Contributions: Methodology, X.L. and X.F.; software, X.L. and N.C.; validation, X.F., G.W. and N.C.; formal analysis, M.L. and G.W.; investigation, G.W. and Y.S.; resources, M.L.; data curation, X.L., N.C. and Y.S.; writing—original draft preparation, X.L.; writing—review and editing, X.L., X.F., M.L. and G.W.; project administration, X.F. All authors have read and agreed to the published version of the manuscript.

Funding: This work was supported by the National Natural Science Foundation of China (Nos. 52474183, 52474186).

Institutional Review Board Statement: Not applicable.

Informed Consent Statement: Not applicable.

Data Availability Statement: All data and code used or analyzed in this study are available from the corresponding author on reasonable request.

Conflicts of Interest: The authors declare no conflict of interest.

References

1. Li, L.; Sun, S.; Wang, J.; Yang, W.; Song, S.; Fang, Z. Experimental study of the precursor information of the water inrush in shield tunnels due to the proximity of a water-filled cave. *Int. J. Rock. Mech. Min. Sci.* **2020**, *130*, 104320. [CrossRef]
2. Li, Z.Q.; Nie, L.; Xue, Y.; Li, W.; Fan, K. Model Testing on the Processes, Characteristics, and Mechanism of Water Inrush Induced by Karst Caves Ahead and Alongside a Tunnel. *Rock. Mech. Rock. Eng.* **2025**, *58*, 5363–5380. [CrossRef]
3. Cheng, W.; Yin, H.; Xie, D.; Dong, F.; Li, Y.; Zhu, T.; Wang, J. Prediction of dominant roof water inrush windows and analysis of control target area based on set pair variable weight—Forward correlation cloud model. *J. Clean. Prod.* **2024**, *483*, 144253. [CrossRef]
4. Qlan, Z.; Sul, W.; Guan, Y. Mechanism and salvage of sand-water mixture inrush induced by roof fallingin deep coal roadway. *J. China Univ. Min. Technol.* **2024**, *53*, 915–924. [CrossRef]
5. Wang, J.; Li, S.; Bai, J.; Zhang, Q. Probabilistic assessment of water inrush risk in coal mines through coupled Monte Carlo and peridynamics. *Tunn. Undergr. Space Technol.* **2023**, *140*, 105289. [CrossRef]
6. Qiushuang, Z.; Changfeng, W.; Zhenhao, Z. Research on the prediction of mine water inrush disasters based on multi-factor spatial game reconstruction. *Geomech. Geophys. Geo-Energy Geo-Resour.* **2024**, *10*, 41.
7. Tang, S.; Fu, X.; Xie, B. Comprehensive Evaluation Method for the Grouting Management Effect of Mine Water Hazards Based on the Combined Assignment of the TOPSIS and RSR Methods. *Appl. Sci.* **2024**, *14*, 10228. [CrossRef]
8. Liu, Z.L.; Chen, X.Y.; Cheng, W.D. A Novel Transitional Element-Based Approach for PD-FEM Coupling: Theoretical Development. *Int. J. Simul. Model.* **2025**, *24*, 321–332. [CrossRef]
9. Qin, M.; Yang, D.; Jia, Y.; Zhou, Y. Peridynamics modeling of hydraulic fracture interaction with natural fractures in fractured rock mass. *Eng. Fract. Mech.* **2024**, *307*, 110299. [CrossRef]
10. Qin, M.; Yang, D.; Chen, W. Numerical Investigation of Hydraulic Fracturing in a Heterogeneous Rock Mass Based on Peridynamics. *Rock. Mech. Rock. Eng.* **2023**, *56*, 4485–4505. [CrossRef]
11. Li, M. *Peridynamic Simulation Method and Application of Hydro-Mechanical Coupling in Fractured Rock Masses Under Dynamic Disturbance*; Shandong University: Shangdong, China, 2023. [CrossRef]
12. Ma, P.-F. *Study on Damage-Seepage Characteristics of Fractured Rock Mass Using Peridynamics Method*; Shandong University: Shangdong, China, 2022. [CrossRef]
13. Shi, H.-T. *Peridynamic Fluid-Solid Coupling Model For Hydraulic Fracturing Process in Rock Strata*; Southeast University: Nanjing, China, 2022. [CrossRef]

14. Zhang, G.-H.; Xie, Z.-Z.; Zhang, B.-W.; Jiao, Y.-Y.; Zou, J.-P.; Wu, J.-Q.; Xiong, F.; Tang, Z.-C. Sources of high-temperature water and gas inrush during tunnel excavation: A case of Bangfu tunnel in Southwest China. *J. Rock. Mech. Geotech. Eng.* **2024**, *16*, 5027–5049. [CrossRef]
15. Dong, F.; Yin, H.; Cheng, W.; Zhang, C.; Zhang, D.; Ding, H.; Lu, C.; Wang, Y. Quantitative prediction model and prewarning system of water yield capacity (WYC) from coal seam roof based on deep learning and joint advanced detection. *Energy* **2004**, *290*, 130200. [CrossRef]
16. Fan, K.; Li, W.; Wang, Q.; Liu, S.; Xue, S.; Xie, C.; Wang, Z. Formation mechanism and prediction method of water inrush from separated layers within coal seam mining: A case study in the Shilawusu mining area, China. *Eng. Fail. Anal.* **2019**, *103*, 158–172. [CrossRef]
17. Sun, J.; Hu, Y.; Zhao, G. Relationship between water inrush from coal seam floors and main roof weighting. *Int. J. Min. Sci. Technol.* **2017**, *27*, 873–881. [CrossRef]
18. Hou, E.; Yan, Y.; Wen, Q.; Che, X.; Miao, Y.; Li, H.; Lu, B. Study on prediction of water inrush hazard in roof of roadway driving. *Coal Sci. Technol.* **2022**, *50*, 110–120. [CrossRef]
19. Yang, T.; Yan, Y.; Zhang, J.; Lin, H.; He, Y.; Zhang, Y.; Gao, S. Study on synergistic water-resisting stability of upper and lower soil layers and bedrock layer in shallow coal seam group. *Coal Sci. Technol.* **2023**, *51*, 234–242. [CrossRef]
20. Zeng, Y.; Zhu, H.; Wu, Q.; Guo, X.; Cui, F.; Pang, Z.; Liu, S.; Yang, W. Research status and prevention and control path of coal seam roof water disaster in China J. *China Coal Soc.* **2024**, *49*, 1539–1555. [CrossRef]
21. Qiao, W.; Liu, M.; Li, L.; Guo, W.; Wang, Q.; Meng, X.; Li, X.; Duan, Z.; Chen, W.; Li, W. Disaster mechanism induced by structure evolution of "water-inrus-hing separation zone" of mining rock mass and prediction method of water inrush from separation layer. *J. China Coal Soc.* **2023**, *48*, 818–832. [CrossRef]
22. Ma, K.; Sun, X.; Tang, C.; Wang, S.-J.; Yuan, F.-Z.; Peng, Y.-L.; Liu, K. An early warning method for water inrush in Dongjiahe coal mine based on microseismic moment tensor. *J. Cent. South. Univ.* **2020**, *27*, 3133–3148. [CrossRef]
23. Qiao, W.; Wang, Z.; Li, W.; Lu, Y.; Li, L.; Huang, Y.; He, J.; Li, X.; Zhao, S.; Liu, M. Formation mechanism, disaster-causing mechanism and prevention technology of roof bed separation water disaster in coal mines. *J. China Coal Soc.* **2021**, *46*, 507–522. [CrossRef]
24. Gao, R.; Yan, H.; Ju, F.; Mei, X.; Wang, X. Influential factors and control of water inrush in a coal seam as the main aquifer. *Int. J. Min. Sci. Technol.* **2018**, *28*, 187–193. [CrossRef]
25. Liu, T.; Xu, D.; Shi, L.; Qu, L.; Ji, K. Trapezoidal collapse model to calculate the height of the overburden collapse zone in coal seam mining: An example from Guo'Jiahe Coal Mine, Western China. *Energy* **2022**, *256*, 124609. [CrossRef]
26. Liu, X. *Deformation Failure Mechanism and Control Technology of Surrounding Rock in Loose Fractured Semi-Coal Rock Development Roadway*; China University of Mining and Technology: Xuzhou, China, 2014.
27. Saltelli, A.; Ratto, M.; Andres, T.; Campolongo, F.; Cariboni, J.; Gatelli, D.; Saisana, M.; Tarantola, S. *Global Sensitivity Analysis: The Primer*; John Wiley & Sons: New York, NY, USA, 2007. [CrossRef]
28. Zhang, Y.; Liu, Q.; Zhang, C.; Zhao, J. Uncertainty quantification of rock mass permeability using Monte Carlo and machine learning. *Int. J. Rock Mech. Min. Sci.* **2022**, *152*, 105137. [CrossRef]
29. Lan, T.; Zhang, H.; Li, S.; Batugina, I.; Batugin, A. Application and Development of the Method of Geodynamic Zoning According to Geodynamic Hazard Forecasting at Coal Mines in China. *IOP Conf. Ser. Earth Environ. Sci.* **2019**, *221*, 012088. [CrossRef]
30. Yang, J.; Peng, C.; Ye, Z.; Yao, C.; Zhang, X.; Ma, Y.; Zhou, C. Study on the efficiency of energy transfer in the blasting with different coupling mediums for deep rock mass excavation. *Eng. Fract. Mech.* **2025**, *319*, 111048. [CrossRef]
31. Wu, Y.; Zhang, X.; Li, Z.; Gao, W.; Xu, Z.; Zhang, Y.; Zhou, J. Effects of In-Situ Stress on Damage and Fractal during Cutting Blasting Excavation. *Fractal Fract.* **2024**, *8*, 450. [CrossRef]
32. Dai, J.; Gong, F.; He, Z.; Xu, L. Quantitative estimation of potential rockburst pit depths during blasting excavation in deep tunnels. *Int. J. Rock. Mech. Min. Sci.* **2024**, *178*, 105748. [CrossRef]
33. Hong, Z.; Tao, M.; Wu, C.; Zhou, J.; Wang, D. The spatial distribution of excavation damaged zone around underground roadways during blasting excavation. *Bull. Eng. Geol. Environ.* **2023**, *82*, 155. [CrossRef]
34. Stauffer, D.; Aharony, A. *Introduction to Percolation Theory*, 2nd ed.; Taylor & Francis: London, UK, 1994.
35. Oterkus, S.; Madenci, E.; Oterkus, E. Peridynamic modeling of anisotropic media. *J. Elasticity* **2023**, *152*, 1–24. [CrossRef]
36. Zimmerman, R.W.; Al-Yaarubi, A. Non-linear regimes of fluid flow in rock fractures. *Int. J. Rock. Mech. Min. Sci.* **2004**, *41*, 163–169. [CrossRef]

Disclaimer/Publisher's Note: The statements, opinions and data contained in all publications are solely those of the individual author(s) and contributor(s) and not of MDPI and/or the editor(s). MDPI and/or the editor(s) disclaim responsibility for any injury to people or property resulting from any ideas, methods, instructions or products referred to in the content.